COMMUNICATION

High-Operating-Temperature Direct Ink Writing of Mesoscale Eutectic Architectures

*J. William Boley, Kundan Chaudhary, Thomas J. Ober, Mohammadreza Khorasaninejad, Wei Ting Chen, Erik Hanson, Ashish Kulkarni, Jaewon Oh, Jinwoo Kim, Larry K. Aagesen, Alexander Y. Zhu, Federico Capasso, Katsuyo Thornton, Paul V. Braun, and Jennifer A. Lewis**

The ability to rapidly fabricate materials with controlled periodicity on length scales near the wavelength of visible light is important for optical devices,[1,2] cloaking,[3–6] beam shaping,[7–11] and other applications. Most optical materials are fabricated using lithographic techniques[12] that provide exquisite control over their composition and feature size. Recently, directional solidification of eutectic materials has been investigated as an alternate approach for fabricating optical devices. Upon cooling from the molten state, these materials self organize into lamellar, rod-like, or other periodic motifs.[13] Remarkably, these structures often bear a striking resemblance to lithographically fabricated photonics[14–16] and metamaterials,[17,18] and, in some cases, exhibit unique structures that give rise to a localized surface plasmon resonance.[19,20] However, despite their promise, scant attention has been given to simultaneously patterning and directionally solidifying eutectic materials.

Here, we report a new process for creating mesoscale eutectic architectures, known as high-operating-temperature direct ink writing (HOT-DIW). Unlike micro-pull-down methods that control directional solidification,[19,20] HOT-DIW also enables direct patterning of eutectic materials. Specifically, we print a molten eutectic ink composed of silver chloride (AgCl)–potassium chloride (KCl) onto a glass substrate in air under ambient conditions. The ink solidifies when cooled below its eutectic temperature ($T_E \approx 319$ °C).[21–23] By controlling the printing temperature and speed, we create mesoscale eutectic AgCl–KCl architectures composed of lamellar features oriented along the printing direction, whose periodic spacing can be systematically varied between approximately 100 nm and 2 µm. Heat transfer calculations and phase field modeling are carried out to understand the influence of key printing parameters on their directional solidification. Given their periodicity, these mesoscale eutectic architectures serve as diffraction gratings that manipulate light in the visible and infrared regimes. By selectively etching KCl lamellae followed by coating silver onto the remaining AgCl lamellae, their diffraction efficiency is enhanced by an order of magnitude. While we focused on the AgCl–KCl system due to its relatively low eutectic temperature, lamellar microstructure, and ability to print in air,[14] HOT-DIW enables patterning of nearly any material whose melting point is below 700 °C, the current maximum hot operating temperature, including polymers, glasses, and metal eutectics (Figure S1, Supporting Information).

The HOT-DIW platform consists of a custom-designed graphite nozzle that is locally heated to 400 °C (i.e., $T_{nozzle} > T_E$) through which the molten AgCl–KCl ink flows (**Figure 1**a). This molten ink consists of a low viscosity (≈2–3 mPa s), Newtonian fluid that undergoes directional solidification upon contact with the cold substrate (held at room temperature). For printing speeds of interest (<1 mm s^{-1}), surface forces play a significant role due to the low capillary number ($C_a \leq 1.2 \times 10^{-4}$) (see the Experimental Section). To produce uniform printed filaments, the applied pressure must not exceed the Laplace pressure at the nozzle-substrate interface, which necessitates a small gap height (10 µm) between the nozzle and the substrate during printing (Figure 1b and Movie S1, Supporting Information). The solidification front trails the hot nozzle, as the nozzle is translated across the substrate at a printing speed, v. Upon solidification of the eutectic ink, the AgCl and KCl phases self-organize into a lamellar architecture (Figure 1c) with a characteristic spacing, L, which is governed by the rates of solidification and diffusion ahead of the solidification front[22] and whose relative lamellar widths are determined by the eutectic composition (i.e., 62% AgCl and 38% KCl by volume).[24]

To demonstrate HOT-DIW, we produced meander line patterns composed of eutectic AgCl–KCl filaments that are nominally 2 mm wide, corresponding to the outer diameter of the nozzle used. The representative eutectic filaments shown in **Figure 2**a are printed at a speed of 0.18 mm s^{-1}. Their curved top surface arises due to surface area minimization of the molten eutectic ink (surface tension, $\sigma \approx 146$ mN m^{-1})[25]

Dr. J. W. Boley, K. Chaudhary, Dr. T. J. Ober, Dr. M. Khorasaninejad, Dr. W. T. Chen, A. Y. Zhu, Prof. F. Capasso, Prof. J. A. Lewis
John A. Paulson School of Engineering and Applied Sciences
Wyss Institute for Biologically Inspired Engineering
Harvard University
Cambridge, MA 02138, USA
E-mail: jalewis@seas.harvard.edu
E. Hanson, Dr. L. K. Aagesen, Prof. K. Thornton
Department of Materials Science and Engineering
University of Michigan
Ann Arbor, MI 48109, USA
A. Kulkarni, Dr. J. Kim, Prof. P. V. Braun
Department of Materials Science and Engineering
Frederick Seitz Materials Research Laboratory
University of Illinois at Urbana-Champaign
Urbana, IL 61801, USA
J. Oh
University of Waterloo
Waterloo, ON N2L 3G1, Canada

DOI: 10.1002/adma.201604778

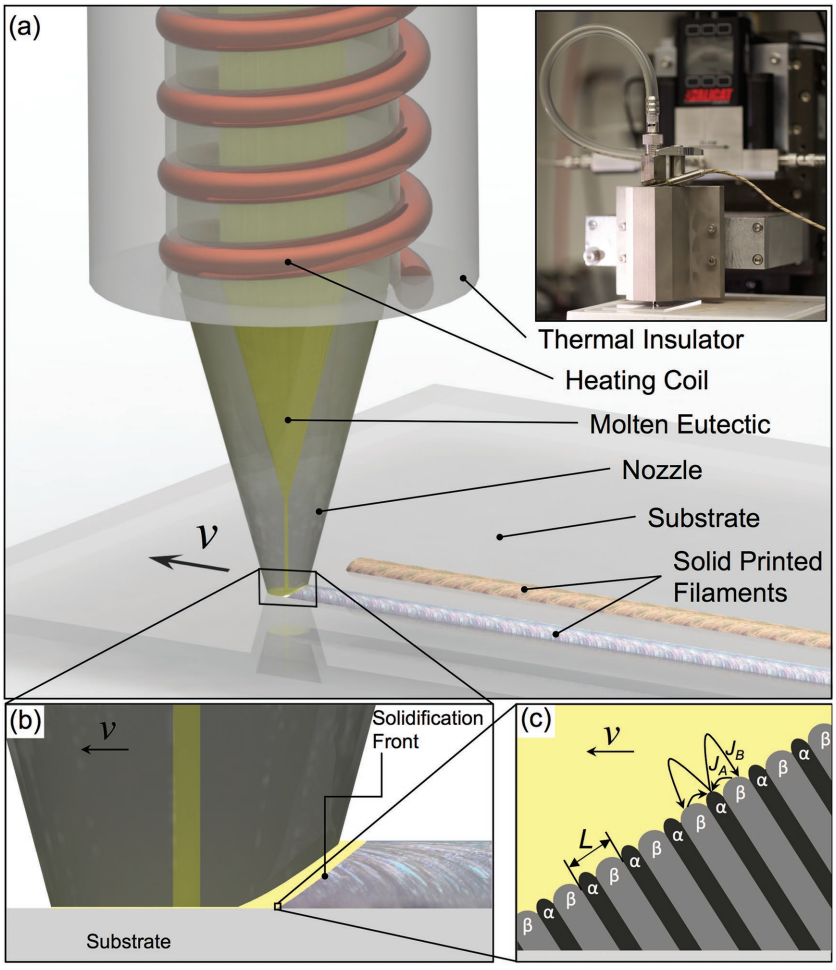

Figure 1. HOT-DIW of molten eutectic inks. a) Overview of printing system and list of components (main) with photograph of system (inset). b) Detail side view schematic of printing process showing the solidification front following the HOT nozzle. The figure is drawn to scale to match the physical process. The nozzle inner diameter is ≈200 µm. c) Microscale schematic of solidification front showing solid–liquid interface and the lamellar growth during the printing process. In this case, the dark lamellae (α-phase) represent KCl and the light gray lamellae (β-phase) represent AgCl. J_A and J_B represent the flux of KCl and AgCl, respectively, into their corresponding solid phases.

prior to solidification, while their flat bottom surface conforms to the underlying substrate. The lamellar features observed on the top and bottom surfaces exhibit long-range order, persisting along the length and through the thickness of the printed filaments (Figure 2b, and Figure S2, Supporting Information). The lamellar spacing (and orientation) measured at the two edges and center region of these filaments are 668 ± 84 nm (70° ± 7°) and 324 ± 32 nm (3° ± 4°), respectively, where the printing direction is defined as 0°. These values are in good agreement with predicted values of 716 nm and 67° (edge) and 309 nm and 0° (center) determined by phase-field modeling.

The lamellar spacing within the printed eutectic architectures can be systematically controlled by varying the printing speed (**Figure 3**). At low speeds ($v \leq v_{crit}$), the printed eutectic filaments exhibit a periodic lamellar architecture, whose characteristic spacing decreases with increasing v (Figure 3a). However, when $v > v_{crit}$, multiple lamellar domains are observed that progress inward from each edge ultimately impinging in the center of the filament (Figure 3a). A transition from a uniform to nonuniform lamellar architecture occurs at v_{crit} (≈ 1 mm s^{-1}). To better understand these experimental observations, 2D heat transfer calculations are carried out to determine the influence of printing speed, v, on the shape and evolution of the solidification front within the printed filaments (Figure 3b and Figure S3a, Supporting Information). When $v \leq v_{crit}$, the temperature field remains constant throughout the thickness of the filament resulting in a vertical solidification front that gives rise to a uniform lamellar architecture (Figure 3b). At v_{crit}, the Péclet number, P_e, is close to unity ($P_e \approx 0.85$) (see the Experimental Section). When $v \leq v_{crit}$, the speed of the solidification front is approximately identical to v. However, this relationship falls off sharply when $v > v_{crit}$ and the temperature field becomes nonuniform throughout the thickness of the filament shifting the solidification front away from the nozzle to the filament edges (Figure 3b). Under these conditions, the solidification front deviates from a vertical orientation (Figure 3b), as the advective heat transfer rate associated with a given printing speed becomes large relative to thermal diffusion through the filament thickness ($P_e > 0.85$). The HOT nozzle moves away from the deposited eutectic ink quickly enough such that its influence on the solidification front lessens as v increases (Figure S3a, Supporting Information). This weaker dependence of the solidification front speed on v translates to a weaker dependence of L on v[22] (Figure 3c). Therefore, above $v_{crit} \approx 1$ mm s^{-1}, the direction of solidification and, hence, lamellar growth changes from predominately parallel to the print path to primarily inward from each filament edge, while remaining vertical to the substrate. As these lamellar features converge at the filament center, domain boundaries arise leading to a nonuniform architecture (Figure 3a). Based on simulations, the printed filaments begin to solidify roughly 200 µm downstream from the HOT nozzle-molten ink interface (Figure 3b).

The lamellar spacing L within the printed eutectic features can be varied from 2.3 µm down to 140 nm as the printing speed, v, is increased up to v_{crit}. These periodic features lie within the range of values required for manipulating light in the visible and infrared regimes. We note that the HOT nozzle imposes a curvilinear high temperature boundary (Figure S3b, Supporting Information) that leads to a gradient in lamellar spacing from the filament edge to its center. We also find that all values of L observed for printed architectures fabricated at $v \leq v_{crit}$ can be collapsed onto a single curve (Figure 3d) that corresponds to the solidification front velocity ($V = v\sin\phi$). Eutectic

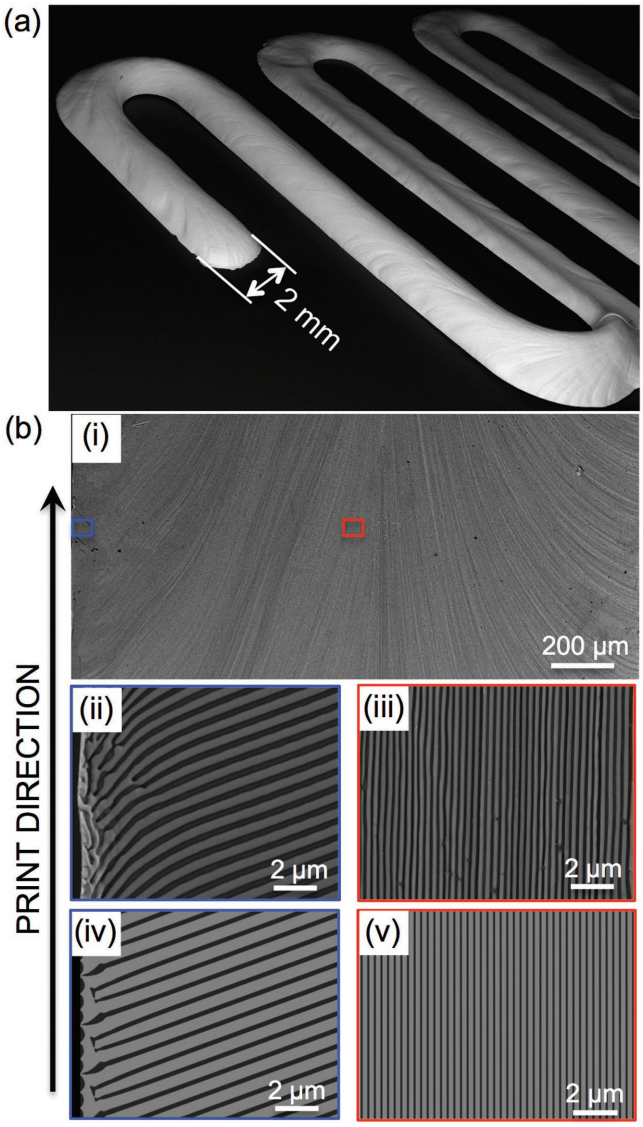

Figure 2. Printed eutectic AgCl–KCl filaments. a) Macroscale SEM image of typical printed meander pattern. b) Representative images of printed filament (bottom surface), including: i) low magnification and ii,iii) high magnification views along with iv,v) corresponding predicted images from phase field modeling of filament edge (blue) and center (red), respectively. The experimental data and simulations correspond to $v = 0.18$ mm s^{-1}.

materials that form lamellar microstructures when solidified with minimum undercooling should exhibit a theoretical spacing L, defined by the power law $L = cV^{-0.5}$, where the constant of proportionality, c, is dependent on the material properties of the system.[22] By fitting our data to this model, we find good agreement with the predicted power law dependence and obtain a value of $c = 5.40 \times 10^{-9} \pm 0.13 \times 10^{-9}$.

The periodic architecture coupled with the precise control over the lamellar spacing achieved in printed filaments fabricated at $v \leq v_{crit}$ make them effective diffraction gratings (**Figure 4**a). The angle-dependent spectra measured from light diffracted from the bottom surface of the filaments follow the same trend as simulations for a model grating (Figure 4b). By varying v (and therefore L), we can tailor the incident angle θ where the central wavelength of the visible spectrum ($\lambda = 515$ nm) is reflected (Figure 4c). The measured and simulated normalized diffraction efficiency (defined as the corresponding reflected signal normalized by the respective maximum reflected over the plotted region) show that the spectrum shifts to larger θ for increased v (decreased L). Further comparison between these experimental results and model predictions can be made by estimating L from the first order diffraction response, where $L = \lambda_{max}/\sin\theta_{fo}$ and λ_{max} is the wavelength at which the normalized diffraction efficiency is maximized for each angle in the first order diffraction, θ_{fo} (Figure S4, Supporting Information). The primary peaks observed experimentally are accompanied by pronounced shoulder peaks that likely arise due to the waviness of the lamellae within the printed filaments (Figure S5, Supporting Information). Light transmitted through the bottom surface of the printed filament would be affected by the wavy interfaces between the two phases, since they each transmit light in the visible range. The measured and simulated absolute efficiencies of the as-printed samples are low (less than 3% in all cases) and follow similar trends (Figure S6a,b, Supporting Information). The modest difference in absolute efficiencies may stem from variations in the lamellar spacing within printed filaments that are not well captured by the simulations. In all cases, their measured angular response is in good agreement with the predicted response (Figure 4b,c). In addition, the estimated values of L from the measured spectra are consistent with those observed directly by scanning electron microscopy (Figure S4, Supporting Information). Notably, we also find that the printed architectures exhibit vivid structural color, which can be tuned by controlling the printing speed (Figure S7 and Movie S2 and S3, Supporting Information).

To further improve the diffraction grating performance, we selectively etched the KCl phase from printed eutectic filaments ($v = 0.05$ mm s^{-1}, $L = 801$ nm). These features are selected to maximize the applicable range of wavelengths and the amount of light diffracted in the first order. The as-printed eutectic filaments exhibit a low diffraction efficiency (<1.6%) (Figure 4d). Upon removing the KCl phase, the diffraction efficiency increased to ≈2.5% due to the increase in refractive index contrast between the resulting air voids and adjacent AgCl lamellae. By depositing a silver coating (450 nm thick) onto the AgCl lamellae, we observed an order of magnitude increase in diffraction efficiency (≈15%) compared to the as-printed gratings. The observed enhancement is in good agreement with their simulated absolute efficiencies (Figure S6c, Supporting Information).

In summary, we introduce a new printing method, HOT-DIW, for patterning eutectic materials for optical applications in the visible and IR regimes. By controlling the print speed, the lamellar spacing within the printed filaments can be systematically varied between approximately 100 nm and 2 μm. Both the as-printed mesoscale architectures and the metallo-dielectric variants templated from those structures may find application as Bragg reflectors. Upon further optimization, this method should allow the programmable patterning of a wide range of materials, including polymers, metal eutectics, and glass, in both large area and multilayer formats.

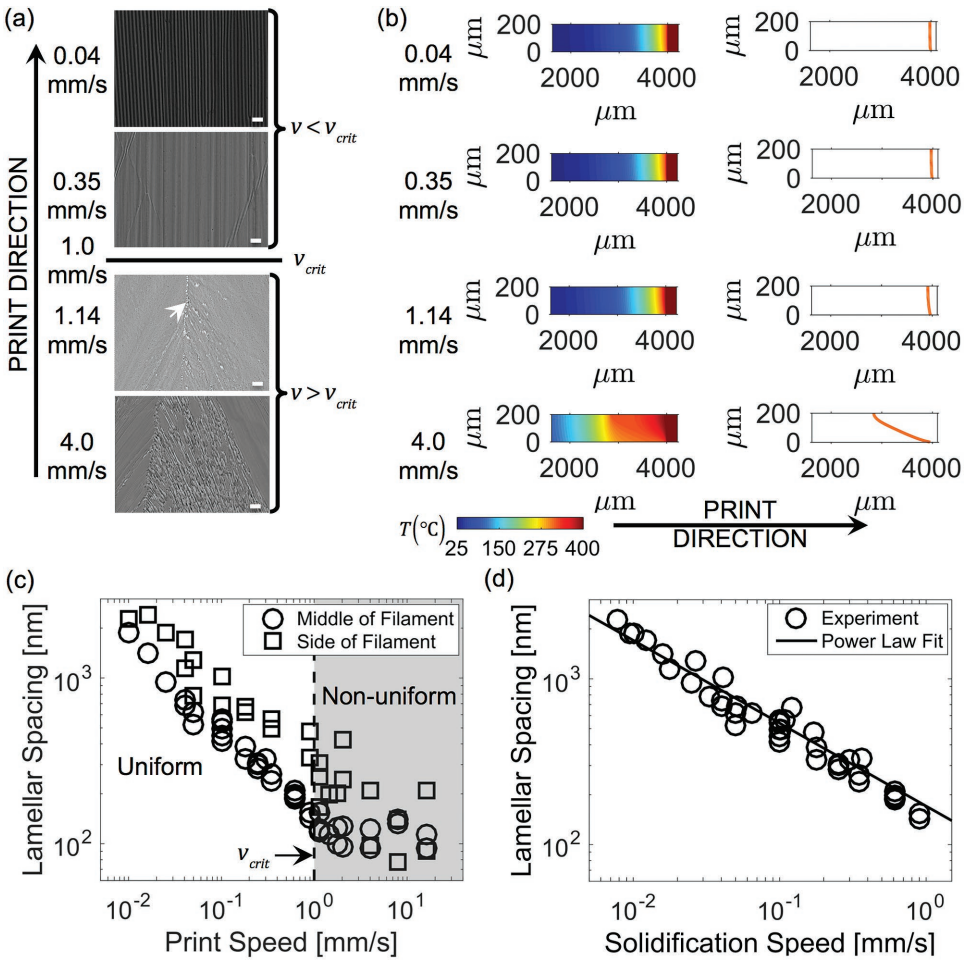

Figure 3. Controlling lamellar spacing in printed eutectic AgCl–KCl filaments. a) SEM images of eutectic filaments (center region, bottom surface) printed at speeds below and above v_{crit}. [Note: The arrow shown in the image at $v = 1.14$ mm s^{-1} denotes the formation of a domain boundary within the printed filament.] Scale bars are 2 μm. b) 2D heat transfer simulations of the central region of printed filaments as a function of printing speed, which reveal the temperature fields (left column) and resulting solidification fronts (right column). The HOT nozzle interface is located at position 4214 μm in the print direction. c) Lamellar spacing measured within the printed filaments as a function of print speed. The white region denotes filaments printed below v_{crit}, where lamellae of uniform orientation are observed. The gray region denotes filaments printed above v_{crit}, which contain lamellae that are nonuniform in orientation. d) Lamellar spacing as a function of solidification front velocity.

Experimental Section

Materials Systems: The eutectic AgCl–KCl ink was prepared by mixing as-received AgCl (99.997%, Alfa Aesar) and KCl (99%, Sigma-Aldrich) powders in a glass petri dish on a mass balance (Mettler AE 50) at 82 and 18 wt% (70 and 30 at%), respectively, corresponding to its eutectic composition.[24] The glass dish was then transferred to a hot plate (Corning PC-6200), heated to 450 °C (confirmed via Cen-Tech Infrared Thermometer, Item 60725) for ≈2 h and air cooled to room temperature for ≈30 min. The solidified eutectic was then ground into a powder via mortar and pestle and loaded into the HOT printhead, which consisted of a heated ink reservoir and custom-designed graphite nozzle. Polymer and metal alloy inks were prepared by cutting as-received poly(lactic acid) (PLA) filament (MakerBot) and Bi-Sn (American Elements, BI-SN01-P.42SN) with metal shears to produce small pellets that fitted into the HOT printhead. The sugar ink was used as-received (Isomalt, Amazon).

HOT-DIW System: The HOT-DIW system was comprised of a HOT printhead mounted to a 3D gantry stage, which moved the printhead relative to a stationary glass substrate (VWR, 2950) that was placed on a hot plate (Fisher Isotmp, 11-800-49SHP). The HOT printhead was comprised of a nozzle contained in steel barrel that was wrapped with a heater coil (FM Keefe Company Inc., 62H36A5X-1128). This assembly was contained within a ceramic sleeve for thermal insulation and inserted into a custom mount that fixed the HOT printhead to the gantry stage. For temperature feedback, a K-type thermocouple was mounted to the HOT printhead assembly with physical contact maintained between the thermocouple bead and the HOT nozzle tip. A camera (UI-3590CP-HQ) with 3.44 magnification was also mounted to the gantry for registering the HOT printhead at its starting position. The temperature of the HOT printhead was achieved via temperature controller (Omega, CNi16). Typical HOT-DIW experiments were conducted by placing a glass substrate (precleaned by rinsing with acetone and drying with house air and then by rinsing with ethanol and drying with house air; each step was repeated three times) onto a base plate (held at room temperature) with Kapton tape, loading the ink into the HOT printhead (≈1.0 g per experiment), moving the HOT printhead to its starting position, and setting the HOT printhead to the desired nozzle temperature. Once the HOT printhead reached a steady-state value, it was pressurized and the meander line patterns were printed at prescribed speeds. For the AgCl–KCl eutectic system, the molten ink was heated to 400 °C and printed at varying speeds at an applied pressure $P_{applied} \approx 0.44$ psi (3.03 kPa)

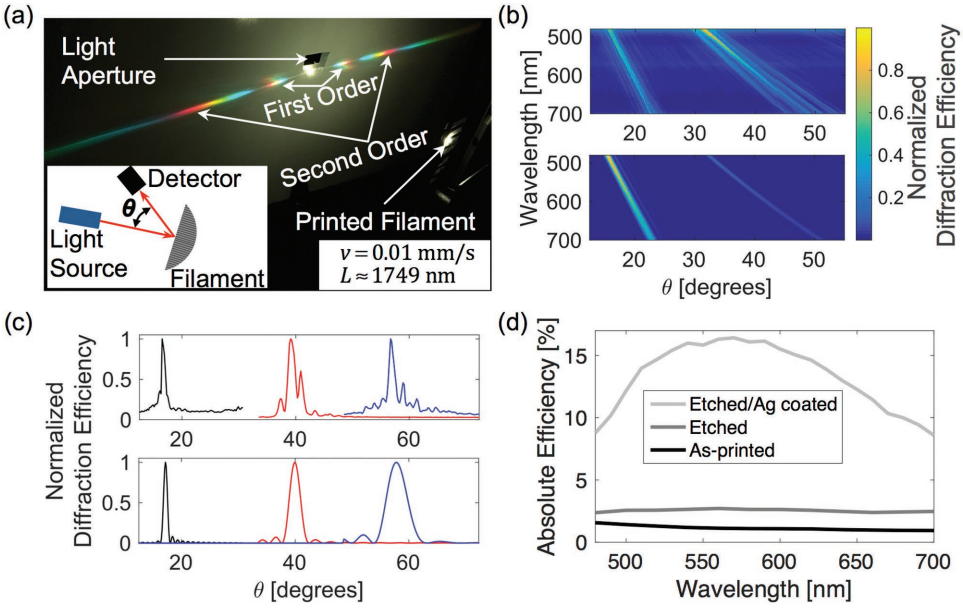

Figure 4. Optical properties of printed, etched, and coated filaments. a) Optical image of diffraction patterns of a broadband light source reflecting off of the bottom surface of a printed eutectic AgCl–KCl filament (main) [Inset shows schematic view of procedure used to measure spectra and efficiency of reflected light.] b) Representative (top) measured and (bottom) simulated spectra of reflected light for a eutectic filament printed at $\nu = 0.01$ mm s^{-1} ($L \approx 1749$ nm). c) (Top) Measured and (bottom) simulated normalized diffraction efficiency of first order for wavelength at center of visible spectrum ($\lambda = 515$ nm) for eutectic filaments printed at $\nu = 0.01$ mm s^{-1} ($L \approx 1749$ nm) (black), $\nu = 0.05$ mm s^{-1} ($L \approx 801$ nm) (red), and $\nu = 0.1$ mm s^{-1} ($L \approx 606$ nm) (blue). d) Measured absolute diffraction efficiency for as-printed ($\nu = 0.05$ mm s^{-1}), KCl-etched, and KCl-etched and coated with silver (450 nm thick), where $L \approx 801$ nm.

through a graphite nozzle (outer diameter = 2 mm, inner diameter ≈200 µm, see Figure S8, Supporting Information). The printed line width was 2 mm for all speeds. The estimated flow rate for these experiments was ≈14 µL min^{-1}. To demonstrate the broader applicability of HOT-DIW, the authors also printed molten PLA, a metallic alloy composed of bismuth-tin (Bi-Sn), and a carbohydrate glass composed of molten sugar through stainless-steel nozzles (Tecdia Inc.) heated to 200 °C onto glass substrates held at room temperature. These PLA, Bi-Sn, and sugar inks were printed at speeds of 5, 10, and 5 mm s^{-1} under applied pressures (Nordson EFD) of 80, 20, and 10 psi, respectively.

Capillary and Péclet Numbers: The relative importance of viscous and surface forces during HOT-DIW of molten eutectic AgCl–KCl inks was determined by the capillary number, $Ca = \mu\nu/\sigma$; where μ is the viscosity of the molten ink (3.1 mPa s), ν is the print speed ($\nu_{max} = 4$ mm s^{-1}), and σ is surface tension (145 mN m^{-1}). Based on these values, the authors calculated an upper bound of $Ca_{max} = 1.2 \times 10^{-4}$. During printing, the molten eutectic wicked up the HOT nozzle thereby increasing the thickness of the as-deposited ink from ≈10 µm (gap height) to ≈200 µm before solidification (see Movie S1, Supporting Information). Molten ink flow ($\sigma \approx 145$ mN m^{-1}) minimized energy at the top (free) surface, as the boundary changes from a constrained to free surface. This transition induced a disturbance in the form of waves (refs. [26] and [27]) that solidified as the molten ink cools leaving behind sinusoidally shaped grain boundaries (defects) between lamellae (Figure S2a-iii, Supporting Information). At the substrate surface, this phenonemon was dampened leading to defect-free lamellae (Figure S2b-iii, Supporting Information). These features could also be seen in the polished cross-section of a representative printed filament (Figure S5, Supporting Information). The curvature of the top surface of the filament arose due to surface area minimization during the printing process. A detailed view at the center of the filament (Figure S5b, Supporting Information) revealed wavy lamellae similar to that of the top surface (Figure S2a-iii, Supporting Information), showing that the waves propagated through the filament. However, only straight lamellae were observed within 2 µm of the bottom surface (Figure S5c, Supporting Information). Since the ink did not readily wet the glass substrate, the width of the printed filaments was defined by the outer diameter of the nozzle. The Laplace pressure at the nozzle orifice (radius $R \approx 100$ µm) could be approximated by $\sigma/R \approx 0.7$ kPa, which was much less than $P_{applied}$. The authors used a small gap height of 10 µm, i.e., below $\sigma/P_{applied} \approx 50$ µm, to prevent the molten eutectic ink from spreading uncontrollably. The authors determined the Péclet number, $P_e = \nu T/\alpha_L$, where T is the filament thickness and α_L is the thermal diffusivity of the liquid eutectic, based on the velocity of the nozzle rather than the velocity of fluid flow. Hence, the authors considered the fluid motion in the reference frame of the nozzle that was translating at the printing speed, which provided the ratio between diffusive and advective heat transfer in this moving frame of reference. Using $\nu = \nu_{crit} \approx 1.0$ mm s^{-1}, $T \approx 0.2$ mm (the average thickness of a typical filament, see Figure S5a, Supporting Information), and $\alpha_L = 2.36 \times 10^{-1}$ mm^2 s^{-1} (see Table S1, Supporting Information) yielded $P_e \approx 0.85$ at ν_{crit}.

Heat Transfer Calculations: The steady-state temperature profile of the center of the filament was simulated by solving an equation that accounted for the thermal diffusion and the velocity due to the moving frame of reference, which followed the motion of the nozzle at a printing speed ν:

$$\frac{\partial \tilde{T}}{\partial \tilde{t}} = \tilde{\alpha}\,\tilde{\nabla}^2\tilde{T} + \tilde{\nu}\frac{\partial \tilde{T}}{\partial \tilde{y}} \tag{1}$$

where $\tilde{T}$ is the temperature, $\tilde{t}$ is the time, and $\tilde{\alpha}$ is the thermal diffusivity. Tildes denoted nondimensionalized variables, which were rescaled by the length scale $W_h = 2.5 \times 10^{-5}$ m and the time scale $\tau_h = 2.5 \times 10^{-3}$ s. W_h and τ_h were on the order of α/ν and α/ν^2, respectively. Temperatures were nondimensionalized by a factor of 1 K. The x-axis was parallel to the width of the filament, the y-axis was parallel to the printing direction, and the z-axis was parallel to the thickness of the filament. The printed filament was treated as a rectangular prism, where the bottom surface ($\tilde{z} = 0$) was in contact with the substrate and was subjected to Newton's law of cooling (Equation (2)):

$$J_{\tilde{z}=0} = \tilde{h}_{sub}\left(\tilde{T}_{\tilde{z}=0} - \tilde{T}_{sub}\right) = -\tilde{k}\frac{\partial \tilde{T}}{\partial \tilde{z}}\Big|_{\tilde{z}=0} \quad (2)$$

where J is the heat flux, $\tilde{h}_{sub}$ is the heat transfer coefficient of the substrate, $\tilde{T}_{sub}$ is the substrate temperature, and $\tilde{k}$ is the thermal conductivity of the eutectic. Equation (2) was used to enforce a Neumann boundary condition at the substrate-filament interface. Neumann boundary conditions were enforced at the edges and top of the filament, replacing h_{sub} and T_{sub} with the heat transfer coefficient to air (h_{air}) and the air temperature (T_{air}) respectively. In the y-direction, no-flux boundaries were applied at the front and back of the filament domain. A cylindrical Dirichlet boundary represented the nozzle and was set to the temperature of the nozzle (T_{nozzle}). This cylinder was centered at the maximum y-coordinate of the filament domain and had an outside diameter of d_{noz}. The diameter of the filament was taken to be 3% greater than the nozzle diameter to account for the slight spreading of the molten ink observed during the printing process. The gap height between the nozzle exit and the substrate was 10 µm.

Thermal properties differed between the molten and solidified AgCl–KCl eutectic material. A smoothly varying function to interpolate between liquid and solid values of the thermal diffusivity $\tilde{\alpha}$ and the thermal conductivity $\tilde{k}$ as a function of temperature was needed for numerical convergence. The interpolation function g was given by:

$$g = \frac{3\left(\tilde{T}-\tilde{T}_s\right)^2}{\left(\tilde{T}_L-\tilde{T}_s\right)^2} - \frac{2\left(\tilde{T}-\tilde{T}_s\right)^3}{\left(\tilde{T}_L-\tilde{T}_s\right)^3} \quad (3)$$

where $\tilde{T}_s$ and $\tilde{T}_L$ are the lower and upper bounds of the temperature range used for the interpolation. For temperatures between $\tilde{T}_s$ and $\tilde{T}_L$, $\tilde{\alpha}$ and $\tilde{k}$ were given by:

$$\tilde{\alpha} = \tilde{\alpha}_s(1-g) + \tilde{\alpha}_L g \quad (4)$$

$$\tilde{k} = \tilde{k}_s(1-g) + \tilde{k}_L g \quad (5)$$

where $\tilde{\alpha}_s$ is the solid thermal diffusivity, $\tilde{\alpha}_L$ is the liquid thermal diffusivity, $\tilde{k}_s$ is the solid thermal conductivity, and $\tilde{k}_L$ is the liquid thermal conductivity. For temperatures below $\tilde{T}_s$, $\tilde{\alpha}=\tilde{\alpha}_s$ and $\tilde{k}=\tilde{k}_s$. For temperatures above $\tilde{T}_L$, $\tilde{\alpha}=\tilde{\alpha}_L$ and $\tilde{k}=\tilde{k}_L$. $\tilde{T}_s$ and $\tilde{T}_L$ were chosen to be 1.25 below and above the eutectic temperature, respectively. This range was minimal while still ensuring numerical convergence. A correction term was added for the latent heat rejected at the solidification front over the same temperature range as the interpolation function g. For temperatures between $\tilde{T}_s$ and $\tilde{T}_L$, Equation (1) becomes:

$$\frac{\partial \tilde{T}}{\partial \tilde{t}} = \tilde{\alpha}\,\tilde{\nabla}^2\tilde{T} + \tilde{v}\left[1+\left(\frac{c_L}{c_s}-1\right)g + \left(\frac{c_L}{c_s}-1\right)\tilde{T}\frac{\partial g}{\partial \tilde{T}} + \frac{L_E}{c_s}\frac{\partial g}{\partial \tilde{T}}\right]\frac{\partial \tilde{T}}{\partial \tilde{y}} \quad (6)$$

where c_s and c_L are the heat capacities of the solid and liquid eutectic, respectively, and L_E is the latent heat for the eutectic mixture.

The physical constants used to parameterize the temperature profile model for AgCl–KCl are summarized in Table S1 (Supporting Information). The model was discretized using a centered finite difference scheme and a forward Euler time stepping scheme. For $\partial\tilde{T}/\partial\tilde{y}$ in the velocity term, an upwinding essentially nonoscillatory scheme was utilized (ref. [28]). The dimensionless grid spacing $\Delta\tilde{x}$ and time step $\Delta\tilde{t}$ were 0.05 and 2.5×10^{-5}, respectively. The code was parallelized via domain decomposition using the message passing interface (MPI) library.

2D simulations of a vertical slice within the central region of the filament were performed under steady-state conditions to determine the solidification front orientation in the y–z plane. This 2D simulation adequately captured the behavior at the center of the filament while allowing for a large number of printing speeds to be explored without incurring a large computational cost. The solidification front orientation was calculated as the angle between the printing direction and the surface normal of the contour curve at the eutectic temperature, averaged over the thickness of the filament.

3D simulations were carried out under steady-state conditions to determine the thermal gradients in the y-direction and the orientation of the solidification front in the x–y plane at the bottom surface of the filament (see Figure S9, Supporting Information). The solidification front orientation was calculated by finding the angle between a linear fit to the contour curve at the eutectic temperature (the solidification front) and the printing direction. The linear fit was applied to the outermost 1% of the filament width to find the solidification front orientation at the edge of the filament and the innermost 1% to one side of the center of the filament width to find the solidification front orientation at the center of the filament. The thermal gradients and solidification front orientations were then used to set up the phase field simulation.

Lamellar Growth Model: Solidification of the AgCl–KCl filaments was simulated using a phase field model developed by Folch and Plapp.[29] The phase of each point in the simulated system was described by three nonconserved order parameters (p_{AgCl}, p_{KCl}, p_L), which were constrained at each point such that $p_{AgCl} + p_{KCl} + p_L = 1$. The order parameters took values of $p_{AgCl} = 1$, $p_{KCl} = 0$, $p_L = 0$ in the solid AgCl phase; $p_{AgCl} = 0$, $p_{KCl} = 1$, $p_L = 0$ in the solid KCl phase; and $p_{AgCl} = 0$, $p_{KCl} = 0$, $p_L = 1$ in the liquid phase (molten AgCl–KCl). The interfaces between phases had order parameter values that vary smoothly between zero and one. The evolution of each order parameter p_i, where the subscript i indicates the AgCl, KCl, or liquid phase, was described by the Allen–Cahn equation:

$$\tilde{\tau}(\vec{p})\frac{\partial p_i}{\partial \tilde{t}} = \tilde{\nabla}^2 p_i + \frac{2}{3}\left[-2p_i(1-p_i)(1-2p_i) + \sum_{j\neq i} p_j\left(1-p_j\right)\left(1-2p_j\right)\right] + \tilde{\lambda}\sum_j \frac{\partial g_j}{\partial p_i}\Big|_{p_{AgCl}+p_{KCl}+p_L=1}\left(\mu A_j - B_j\right) \quad (7)$$

where all interfacial energies between the three phases are assumed to be equal. Here, $\tilde{\tau}$ is the relaxation time, $\tilde{t}$ is the simulation (dimensionless) time, $\tilde{\lambda}$ is a coupling constant, g_i is a tilting function which raises the energy well of phase i, and A_i and B_i are the equilibrium concentration and equilibrium chemical free energy for phase i, respectively. Tildes again indicate dimensionless variables. The derivation of this Allen–Cahn equation was described in detail by Folch and Plapp.[29]

The evolution of the chemical composition at each point in the system was calculated using the diffusion equation. Writing the diffusion equation in terms of the chemical potential and including an antitrapping current explained by Folch and Plapp[29] gives:

$$\frac{\partial \mu}{\partial \tilde{t}} = \tilde{\nabla}\cdot\left(\tilde{D}p_L\tilde{\nabla}\mu\right) - \sum_{i=AgCl,KCl} A_i\frac{\partial p_i}{\partial \tilde{t}} + 2a\sum_{i=AgCl,KCl}\left(A_i - A_L\right)\left(-\hat{n}_L\cdot\hat{n}_i\right)\tilde{\nabla}\cdot\left(\hat{n}_i\frac{\partial p_i}{\partial \tilde{t}}\right) \quad (8)$$

where $\tilde{D}$ is the diffusion coefficient, $a = 1/\left(2\sqrt{2}\right)$, and $\hat{n}_i$ is the unit vector normal to the interface of phase i. The scaled dimensionless equilibrium concentration of phase i is defined as $c_i = (C_i - C_E)/\Delta C$ where C_i is the molar fraction KCl equilibrium concentration of phase i, C_E is the eutectic point concentration, and ΔC is the difference in the equilibrium concentrations of the two solid phases (in this case, $\Delta C = 1$).

Phase transformations in the phase field model were driven by changes in the free energy landscape with changing temperature. The terms that defined the temperature dependence of the free energy curves (A_i and B_i) varied from those described by Folch and Plapp[29] because of the lack of any solubility of KCl in the AgCl solid phase and vice versa. A_i and B_i and were defined as given by Equation (9) and (10):

$$A_i = c_i - \frac{\left(\tilde{y} - \tilde{v}\tilde{t} - \tilde{y}_{int}(x)\right)\tilde{G}}{m_i\Delta C} \quad (9)$$

$$B_i = A_i \frac{\left(\tilde{y} - \tilde{v}\tilde{t} - \tilde{y}_{\text{int}}(x)\right)\tilde{G}}{m_i \Delta C} \quad (10)$$

The *x*- and *y*-directions are the same as those defined in the temperature profile model, v is the printing velocity, and $\tilde{G}$ is the thermal gradient along the *y*-direction, and m_i is the liquidus slope for phase *i*. $\tilde{y}_{\text{int}}(x)$ is the initial position in the *y*-direction of the eutectic temperature isotherm as a function of x. $\tilde{y}_{\text{int}}(x)$ is based on the shape of the solidification front calculated by the temperature profile model. Since only the relative difference between A_i and A_L was relevant, the authors set $A_L = 0$ and $B_L = 0$.

The physical constants used to parameterize the model for the AgCl–KCl system are provided in Table S1 (Supporting Information). Note that the thermal gradient for simulations of the edge of the filament used a thermal gradient that was higher than that calculated by the temperature profile method (1.5×10^7 K m^{-1}) to encourage nucleation of new lamellae. A higher thermal gradient was expected because the experiment showed a curved surface in which the filament edge became thin, a feature not captured in the temperature profile model. A centered finite difference scheme with forward Euler time stepping was used to discretize the model. Variables are nondimensionalized using the length scale W_p and time scale τ_p. W_p is chosen such that the ratio between the expected lamellar spacing and W_p was at least 64; τ_p was the average of the relaxation times of the AgCl and KCl phases as described by Folch and Plapp.[29] The current phase field model did not account for the differences in molar volume between AgCl and KCl. Therefore, the volume fraction of the simulated microstructure took the same value as the molar fraction (70% AgCl/30% KCl), rather than the actual volume fraction (62% AgCl/38% KCl). However, the authors did not believe that the morphology was significantly affected by this discrepancy because of the system's tendency to form lamellar features.

For the center of the filament, $W_p = 5.0625 \times 10^{-9}$ m and $\tau_p = 3.78 \times 10^{-8}$ s. For the edge of the filament, $W_p = 1.0125 \times 10^{-8}$ m and $\tau_p = 3.03 \times 10^{-7}$ s. Greater values of W_p and τ_p were used for the edge of the filament, because the lamellar feature size was larger. The dimensionless grid spacing $\Delta\tilde{x}$ was 0.8 and the time step $\Delta\tilde{t}$ was 2.29×10^{-2} for the center and 1.15×10^{-2} for the edge. Simulations of the center of the filament used periodic boundary conditions in the *x*-direction because the isotherm was parallel with the *x*-axis; while simulations of the edge of the filament used no-flux boundaries in the *x*-direction. In both cases, no-flux boundaries were used in the *y*-direction. The code was parallelized by way of domain decomposition using the MPI library.

An initial set of AgCl–KCl lamellae with a small periodicity of 32.4 nm (on the order of one tenth of the experimentally observed spacing) was used to allow lamellar merging so that a natural lamellar spacing evolved at steady state. The initial lamellar spacing was perturbed by 5%. The initial lamellar pairs had spacings varying randomly by 5% to break the symmetry of the initial conditions and allowed for a less constrained evolution. The initial solidification front was set to have the same orientation as eutectic temperature isotherm with some initial estimate for the undercooling (set by the distance in the *y*-direction between the solidification front and eutectic isotherm). The initial concentration of the liquid was uniformly at the eutectic concentration. The simulation domain shifted to follow the solidification, discarding the coldest row of gridpoints in the solid and adding a row to the hottest part of the liquid each time the solidification front progresses by one gridpoint in the *y*-direction. The simulations were continued until a stable microstructure was observed.

Printed Filament Microstructures: High magnification images of the printed AgCl–KCl eutectic filaments were obtained using a Zeiss Ultra Plus Field Emission scanning electron microscope (FESEM). The procedure to determine L and ϕ was as follows. First, the images were captured so that the print direction of the filaments was aligned with the vertical edge of the SEM field of view. Next, SEM images were acquired in the middle and side of the filament at appropriate magnifications for distinguishing separate phases of the lamellae. Image analysis was carried out using an in-house matrix laboratory (MATLAB) script based on a 2D fast Fourier transform in the spatial domain to determine the average L and ϕ for each image. Eutectic composition and KCl phase etching were confirmed via energy-dispersive X-ray spectroscopy (Zeiss Supra55VP FESEM) (see Figure S10 and S11, Supporting Information, respectively). The large field of view SEM featured in Figure 2a was obtained by mounting the sample to an aluminum pin mount using conductive carbon tape and imaging with a Tescan Vega3 GMU SEM.

KCl Phase Etching and Replacement: To etch the KCl phase, the printed filaments were immersed into an ethanol bath for 30 min. The etched filaments were then removed from the bath and air dried with a light stream of house air. The resulting etch depth was ≈2.5 µm (Figure S12, Supporting Information). If desired, a silver (Ag) coating was then deposited using electron beam evaporation at a rate of 3 Å s^{-1} at a pressure of 1×10^{-6} Torr. A fast rate of deposition was used to minimize localized island formation in the Ag film growth process. No adhesion layer was used in this process to avoid affecting the optical properties of the device.

Optical Measurements: Grating efficiency measurements were obtained using a light source, which consisted of a fiber-coupled tunable laser (SuperK Varia). The beam was collimated by a fiber-coupled collimator (Thorlabs RC12APC-P01) with a beam size diameter of 1 cm and passed through a Glan–Thompson polarizer (Thorlabs GTH10). The collimated beam was focused on the sample with a plano-convex lens with focal length of 15 cm resulting in a Gaussian beam with full width at half maximum of 100 µm. The optical power of the diffracted beam was measured in reflection mode by an optical power meter. The input wavelength was swept from 480 to 700 nm and accordingly the optical power meter position was adjusted to measure the diffraction efficiency of the grating (due to change in the grating diffraction angle with wavelength). Diffraction efficiency was defined as the ratio of optical power of the diffracted beam to that of the incident beam. Grating angular distributions were measured as follows. The authors mount a multimode fiber paired with a spectrometer (OceanOptics USB4000 UV–vis) on a rotation stage to measure the angular distribution of far-field reflection from the grating under broadband illumination. The rotation stage was moved by steps of 0.2° to collect the diffracted beam by the fiber and sent it to the spectrometer. The method for measuring the local spectra reflected by the top of the filaments was as follows. The local spectra were measured by putting a multimode fiber (600 µm diameter), which connected to a spectrometer (Ocean USB4000), at the image plane of a Zeiss microscope system (Discovery V20 with an AxioCam ERc 5s camera and a CL 1500 ECO light source). The use of the multimode fiber could filter the unwanted background allowing to measure the spectrum of ≈175 µm × 175 µm area of a sample. The measured spectra were normalized to a reference signal obtained by replacing our sample with an aluminum mirror.

Optical Simulations: The diffraction spectra and absolute efficiencies were calculated using a finite-difference time-domain (FDTD) simulation (using the commercial software from Lumerical, Inc.). The refractive index data of AgCl and KCl[30–32] were fitted with the multicoefficient model (six coefficients) in the wavelength range 400–800 nm setting the imaginary components as 0. The refractive indices for Ag were taken from the experimental results of Johnson and Christy.[33] The calculations for the reflection diffraction grating were done on an ideal lamellar structure, applying periodic boundary conditions, with its lamellar period as obtained from the SEM analysis of the as-printed eutectic AgCl–KCl filaments. For the etched filaments, KCl was replaced by air, and for the Ag-coated case, a uniformly thick layer of Ag was placed on top of the AgCl layer. Perfectly matched layer (PML) absorbing boundary conditions were applied in the direction of propagation, and the physical structure (2 µm thick) was extended up to this PML boundary. Simulations were performed for normal incident plane waves polarized perpendicularly to the grating period, and far-field projection was used from the reflection monitors. The angle dependent far-field projections were obtained using high-resolution top-hat illumination, taking 20 periods. The far-field projection data of the diffraction grating were normalized to the highest intensity within the 1st and 2nd order regime.

Supporting Information

Supporting Information is available from the Wiley Online Library or from the author.

Acknowledgements

This material is based upon work supported by the Air Force Office of Scientific Research Multidisciplinary University Research Initiative (MURI) FA9550-12-0471. A.K. would like to thank Daniel Bacon-Brown for discussions and help with the FDTD simulations. E.H. and K.T. acknowledge the computational resources from the DoD High Performance Modernization Program and from the University of Michigan's Advanced Research Computing. The authors would also thank Dr. J. Weaver for SEM assistance and Dr. L. Sanders for assistance with photography and videography. J.A.L. gratefully acknowledges support from the Vannevar Bush National Security Science and Engineering Faculty Fellowship (Office of Naval Research (ONR) Award No. N00014-16-1-2823).

Received: September 5, 2016
Revised: October 28, 2016
Published online: December 15, 2016

[1] H. A. Atwater, *Sci. Am.* **2007**, *296*, 56.
[2] C. M. Lieber, *MRS Bull.* **2003**, *28*, 486.
[3] D. Schurig, J. J. Mock, B. J. Justice, S. A. Cummer, J. B. Pendry, A. F. Starr, D. R. Smith, *Science* **2006**, *314*, 977.
[4] J. Valentine, J. Li, T. Zentgraf, G. Bartal, X. Zhang, *Nat. Mater.* **2009**, *8*, 568.
[5] M. Selvanayagam, G. V. Eleftheriades, *Phys. Rev. X* **2013**, *3*, 041011.
[6] X. Ni, Z. J. Wong, M. Mrejen, Y. Wang, X. Zhang, *Science* **2015**, *349*, 1310.
[7] N. Engheta, *Science* **2007**, *317*, 1698.
[8] N. Yu, P. Genevet, M. A. Kats, F. Aieta, J.-P. Tetienne, F. Capasso, Z. Gaburro, *Science* **2011**, *334*, 333.
[9] X. Ni, N. K. Emani, A. V. Kildishev, A. Boltasseva, V. M. Shalaev, *Science* **2012**, *335*, 427.
[10] D. L. Sounas, C. Caloz, A. Alù, *Nat. Commun.* **2013**, *4*, 2407.
[11] A. Silva, F. Monticone, G. Castaldi, V. Galdi, A. Alù, N. Engheta, *Science* **2014**, *343*, 160.
[12] S. H. Kang, M. D. Dickey, *MRS Bull.* **2016**, *41*, 93.
[13] M. N. Croker, R. S. Fidler, R. W. Smith, *Proc. R. Soc. London, Ser. A* **1973**, *335*, 15.
[14] J. Kim, L. K. Aagesen, J. H. Choi, J. Choi, H. S. Kim, J. Liu, C.-R. Cho, J. G. Kang, A. Ramazani, K. Thornton, P. V. Braun, *Adv. Mater.* **2015**, *27*, 4551.
[15] M. Massaouti, A. A. Basharin, M. Kafesaki, M. F. Acosta, R. I. Merino, V. M. Orera, E. N. Economou, C. M. Soukoulis, S. Tzortzakis, *Opt. Lett.* **2013**, *38*, 1140.
[16] R. I. Merino, M. F. Acosta, V. M. Orera, *J. Eur. Ceram. Soc.* **2014**, *34*, 2061.
[17] D. A. Pawlak, K. Kolodziejak, S. Turczynski, J. Kisielewski, K. Rożniatowski, R. Diduszko, M. Kaczkan, M. Malinowski, *Chem. Mater.* **2006**, *18*, 2450.
[18] D. A. Pawlak, S. Turczynski, M. Gajc, K. Kolodziejak, R. Diduszko, K. Rozniatowski, J. Smalc, I. Vendik, *Adv. Funct. Mater.* **2010**, *20*, 1116.
[19] K. Sadecka, M. Gajc, K. Orlinski, H. B. Surma, A. Klos, I. Jozwik-Biala, K. Sobczak, P. Dluzewski, J. Toudert, D. A. Pawlak, *Adv. Opt. Mater.* **2015**, *3*, 381.
[20] K. Sadecka, J. Toudert, H. B. Surma, D. A. Pawlak, *Opt. Express* **2015**, *23*, 19098.
[21] J. D. Hunt, K. A. Jackson, *Trans. Metall. Soc. AIME* **1966**, *236*, 843.
[22] K. A. Jackson, J. D. Hunt, *Trans. Metall. Soc. AIME* **1966**, *236*, 1129.
[23] J. D. Hunt, K. A. Jackson, *Trans. Metall. Soc. AIME* **1967**, *239*, 864.
[24] E. Fischer, *J. Phase Equilib.* **2003**, *24*, 228.
[25] G. J. Janz, R. P. T. Tomkins, C. B. Allen, J. R. Downey, G. L. Garner, U. Krebs, S. K. Singer, *J. Phys. Chem. Ref. Data* **1975**, *4*, 871.
[26] E. Jens, V. Emmanuel, *Rep. Prog. Phys.* **2008**, *71*, 036601.
[27] L. Rayleigh, *Proc. London Math. Soc.* **1878**, *s1–s10*, 4.
[28] S. Osher, *Level Set Methods and Dynamic Implicit Surfaces*, Springer, New York **2003**.
[29] R. Folch, M. Plapp, *Phys. Rev. E* **2005**, *72*, 011602.
[30] L. W. Tilton, E. K. Plyler, R. E. Stephens, *J. Opt. Soc. Am.* **1950**, *40*, 540.
[31] H. H. Li, *J. Phys. Chem. Ref. Data* **1976**, *5*, 329.
[32] M. N. Polyanskiy, Refractive Index Database, http://refractiveindex.info (accessed: March 2016).
[33] P. B. Johnson, R. W. Christy, *Phys. Rev. B* **1972**, *6*, 4370.